1-15-2024

Polymerizing actin regulates myosin-independent mechanosensing by modulating actin elasticity and flow fluctuation

Nikhil Mittal

Etienne Michels

Kathleen Pakenas

Shaina P. Royer-Weeden

Sangyoon J. Han

Follow this and additional works at: https://digitalcommons.mtu.edu/michigantech-p2

 Part of the Biomedical Engineering and Bioengineering Commons, and the Mechanical Engineering Commons

Polymerizing actin regulates myosin-independent mechanosensing by modulating actin elasticity and flow fluctuation

Nikhil Mittal
Michigan Technological university
Etienne Michels
Michigan Technological University
Kathleen Pakenas
Michigan Technological University
Shaina Royer
Michigan Technological University
Sangyoon Han (sjhan@mtu.edu)
Michigan Technological University

Article

Keywords:

Posted Date: June 9th, 2023

DOI: https://doi.org/10.21203/rs.3.rs-2679496/v1

Additional Declarations: There is **NO** Competing Interest.

Version of Record: A version of this preprint was published at Communications Materials on January 15th, 2024. See the published version at https://doi.org/10.1038/s43246-024-00444-0.

Abstract

The stiffness of the extracellular matrix induces differential tension within integrin-based adhesions. However, it has been unclear if the stiffness-dependent differential tension is induced solely by myosin activity. Here, we report that in the absence of myosin contractility, 3T3 fibroblasts still transmit stiffness-dependent differential levels of traction. This myosin-independent differential traction is regulated by polymerizing actin assisted by actin nucleators Arp2/3 and formin where formin has stronger contribution than Arp2/3. Interestingly, we report a four-fold reduction in traction of cells when both Arp2/3 and myosin were inhibited, compared to cells with only myosin inhibition, while there was only a slight reduction in F-actin flow speed in those cells. We show that the conventional rigid-actin-based clutch model is insufficient to explain this force-flow behavior and requires the inclusion of F-actin's own elasticity into consideration. Our model prediction suggests that Arp2/3 and formin modulate stiffness sensing via stiffening F-actin network with stronger effect from formin. Analysis of F-actin flow reveals stiffness-dependent fluctuation frequency in the flow speed, which is predictable only via the model considering actin elasticity. Our data and model provide a potential role of the polymerizing actin and its elasticity in myosin-independent mechanosensing.

Main

Mechanical stiffness of the extracellular matrix (ECM) plays a critical role in regulating many cellular functions such as spreading[1,2], differentiation[3], proliferation[4,5] and migration[6]. In response to the ECM stiffness, different amount of mechanical tension is applied through integrin-based focal adhesions (FAs), which triggers the different levels of conformational opening of mechanosensitive proteins such as talin and vinculin[7–10]. Indeed, multiple studies have found that cell-ECM adhesion transmits increasing traction in response to an increasing ECM stiffness[11–13], which we term 'stiffness-dependent differential traction'. To provide mechanistic understanding about the stiffness-dependent differential traction transmission, non-muscle myosin-II contractility has been suggested as the main force-generator in many conceptual/multiphysics models[14–19] including the molecular clutch model[14–19]. In addition to its role as a force generator, however, myosin II is also a major effector in response to the signals generated from mechanotransduction. Differential tension triggers the integrin-signaling such as RhoA-ROCK pathways[20,21] or Ca^{2+} - MLC kinase pathway[22], which all activates myosin contractility by phosphorylating myosin light chain[23]. Additionally, the tension in F-actin, which would be proportional to the tension in FAs, promotes myosin's localization to F-actin itself[24] and prevent dissociation from F-actin[25]. Myosin-II activation and the force from it promotes cytoskeletal reinforcement and maturation of nascent adhesions to stronger FAs by recruiting other signaling and structural proteins[26]. Thus, myosin might be further activated in response to signaling from differential tension, which is again from myosin-based F-actin flow and clutching. This aspect, i.e., the dual roles of myosin as both an input and an output of stiffness sensing, complicates the understanding of the true source of the stiffness-dependent differential traction transmission.

As an alternative power source, actin assembly at the barbed end of F-actin can induce the retrograde flow by pushing the membrane and being pushed by the membrane, which transmits the traction via cell-ECM adhesions[27]. Myosin-II-inhibited cells are able to transmit small but significant traction force[28,29]. Indirect evidence also shows myosin-inhibited embryonic fibroblasts exert traction seemingly increasing with the substrate stiffness[30]. In the absence of myosin activity, adherent cells also have been shown to exhibit increasing level of cell spreading in response to increasing ECM stiffness with denser adhesion assembly[31,32]. These findings suggest a possibility where the differential tension might be developed in cell-ECM adhesions in response to the ECM stiffness solely by actin polymerization-based retrograde flow and clutch via them. The two mediators for actin polymerization are actin-related-protein 2/3 (Arp2/3) complex and formin homology protein[33,34]. The Arp2/3 complex mediates to form branched actin filaments at the cell membrane[35]. formin promotes actin polymerization by elongating F-actin while remaining at the F-actin's growing barbed ends[36]. Both Arp2/3 and formin mediate advance of F-actin network in a coordinated fashion[37]. However, how they regulate the tension at cell-ECM adhesions have not been unclear. We thus hypothesize that myosin-independent traction comes from the actin-polymerization-driven retrograde flow and the force transmission is regulated by Arp2/3 and formin in a distinct manner.

To test this hypothesis, we have systematically investigated myosin-II and actin nucleators for their roles in differential force transmission in response to the ECM stiffness. We have also developed a modified molecular clutch model which takes into account the role of polymerizing actin and its elasticity in stiffness-dependent differential force transmission in a myosin-independent manner. We show that stiffness-dependent traction transmission is still present without myosin activity and it is governed by actin polymerization mediated by Arp 2/3 and formin. We show that the force sensitivity to the ECM stiffness gradually decreases as we inhibit functions of Arp2/3, formin and actin polymerization itself in addition to myosin inhibition. Via the new model, we demonstrate that actin nucleators participate in mechanosensing by modulating the actin's elasticity. We further provide evidence of the new model by showing fluctuation of the actin flow that relies on the ECM stiffness.

Stiffness-dependent differential force transmission is independent of myosin-II activity

To confirm the stiffness-force relationship in wild-type (WT) cells, we measured the traction of NIH 3T3 fibroblasts plated on a high-refractive-index silicone gel, coated with 40 nm-diameter fluorescent beads and fibronectin, with varying elastic moduli, e.g., 0.6 to 12.7 kPa. The bead images were analyzed for deformation and traction using correlation-based particle tracking velocimetry with re-tracking (cPTVR)[38] and L2-regularized fast boundary element method (FastBEM)[39,40] with an L-curve-based selection of an optimal regularization parameter, respectively[40,41]. The average traction over the cell periphery, *i.e.*, 2 μm in width along the cell edge, where integrin adhesions are usually present, was found to increase with the gel stiffness (Fig. 1a). Specifically, a linear increase was observed up to 2.6 kPa, after which the average

traction plateaued at stiffer regime in 6 and 12.7 kPa (Fig. 1a), overall following a power-law relationship (adj. R^2 = 0.99; Supplementary Table 1). This stiffness-dependent traction trend is consistent with data from previous studies[11–13, 18], and we term it as 'stiffness-dependent differential traction'. As previously observed[11], high tractions were mostly located at cell periphery, which increased in response to the stiffness (Fig. 1b).

To test whether the stiffness-dependent differential traction still exists in absence of myosin-II activity, we treated the cells with 20 μM of blebbistatin (BBS), myosin ATPase inhibitor[42,43], and measured the traction of the cells on gels with the same range of the gel stiffness. This BBS concentration has been shown to effectively suppress the myosin-generated traction in other fibroblasts[44,45], above which has caused a cytotoxic effect[46] (Supplementary Note 1). The inhibition significantly reduced the magnitude of the traction overall, as expected (Fig. 1a, a *gray line*). The ratio of reduction was more substantial in the stiff regime (6-12.7 kPa, ~ 20%) than in the intermediate (1.3–2.6 kPa, ~ 23%) and softer regime (0.6 kPa, ~ 31%) (Extended Data Fig. 1). Interestingly, however, the myosin-inhibited cells still exhibited the stiffness-dependent differential traction with a power-law trend (Fig. 1c) (adj. R^2 = 0.98; Supplementary Table 1). The traction was distributed spatially similar to those shown by WT cells, i.e., inward and concentrated near cell edges (Fig. 1d), implicating myosin-inhibited traction is transmitted through integrin-based adhesions. Taken together, this result demonstrates that the stiffness-dependent differential traction is myosin-independent.

F-actin retrograde flow speed decreases with increasing ECM stiffness in the presence and absence of myosin contractility

F-actin retrograde flow is a major input to the traction transmission[29]. To evaluate how much myosin activity affects the actin flow as a function of the ECM stiffness, we labeled F-actin in NIH 3T3 fibroblasts using SNAP-tag, visualized only a subset of them using a low SNAP substrate concentration[47], and analyzed the actin movies of single cells with quantitative fluorescence speckle microscopy software (qFSM)[47,48] for the actin flow field (Supplementary Movies 1–5). As expected, WT cells showed an inverse relationship of the actin flow speed (V) with the stiffness (E), *i.e.*, a decreased flow speed with increasing stiffness, followed by little change at high stiffness (Fig. 1e). A negative exponential function could well-represent this behavior (Fig. 1e, $V = aexp\left(R_oE\right) + V_o$ where *a*, R_o and V_o are fit constants). Most of the high flow velocity vectors were present at the leading edge of lamellipodia, *e.g.*, ~ 1 μm width along the cell periphery (Fig. 1f, Supplementary Fig. 1) whereas there was a huge reduction in the flow speed at cell-inner area further apart (> 1 μm) from the cell edge (Supplementary Fig. 1a.). This WT actin flow trend is consistent with a previous result with mouse embryonic fibroblasts (MEFs), which, when combined with the molecular clutch model, implies that the stiffness-dependent differential traction is flow-dependent[18].

Similarly to WT cells, the BBS-treated cells also showed a downward trend in flow speed with increasing gel stiffness, followed by little change after 2.6 kPa (Fig. 1g, Supplementary Movies 6–10). The

magnitudes of both the initial downward rate (constant A in the equation at Fig. 1g) and the exponential rate (constant R_o) decreased compared to those in WT (Supplementary Table 2). Despite this reduction, the negative exponential trend demonstrates that the stiffness-dependent differential traction is associated with the actin flow dynamics. As in WT (Fig. 1f), high flow speed regions were mostly at the 2 μm-width layer from the cell edge (Fig. 1h). Together, these results suggest that the traction existing in the absence of myosin II activity is stiffness-dependent and also flow-dependent.

Actin polymerization by Arp2/3 and formin contributes to stiffness-dependent differential traction

Besides myosin contractility, actin polymerization can also generate the F-actin retrograde flow by propelling the cell plasma membrane and being pushed back by the membrane tension[49]. Inhibition of actin polymerization has been shown to result in reduction in traction force in many types of cells[51,52,53] including fibroblasts[50]. However, the relative contribution of actin polymerization to traction force by fibroblasts and its potential dependency on the ECM stiffness have been unknown. To find whether and how much actin polymerization regulates stiffness-dependent, myosin-independent traction transmission, we treated cells, in addition to myosin inhibition with BBS, with CK666 or SMIFH2, inhibitors for Arp2/3 or formin, the two main nucleators of F-actin[54], or with Latrunculin-A, which inhibits actin polymerization and promotes actin depolymerization, and measured the traction of the cells 1 hour after treatment. We disregarded the additional potential effect of SMIFH2 on myosin-II inhibition[55] because we used a low-enough concentration of SMIFH2 and we anyway applied it along with direct myosin inhibition could be disregarded because with BBS.

Cells treated with both CK666 and BBS have shown huge reduction (~ 70%) in traction across the stiffness range compared to cells treated with only BBS (Fig. 2a,g), confirming that Arp2/3-mediated actin polymerization contributes to traction transmission. However, cells with this double-inhibition still showed a monotonic increase in traction with increasing stiffness (Fig. 2a,b). Treatment of cells with CK689, the inactive control for CK666, in addition to BBS exhibited increasing stiffness-force trend (Supplementary Fig. 2) as in BBS-only condition with minimal reduction in the traction. When formin was inhibited in addition to myosin using SMIFH2, cells showed further reduction in traction by ~ 40% compared to myosin-and-Arp2/3 inhibition (Fig. 2c,h). Yet, these cells still showed the stiffness-dependent differential traction (Fig. 2c,d). Most of the traction in both double-inhibited cells was distributed along the periphery of the individual cells, where major F-actin retrograde flow takes place[48,56] (Fig. 2b,d), suggesting that the traction is transmitted via cell-ECM adhesions via molecular clutch mechanism.

To identify a full contribution from actin polymerization to myosin-independent stiffness sensing, we abrogated actin polymerization by treating the cells with Latrunculin-A, which not only sequesters actin monomer (G-actin) but also accelerated F-actin depolymerization[57], along with BBS. This inhibition further decreased the average traction, to a level slightly smaller than one by formin-myosin-inhibited cells, except for one stiffness (6 kPa) condition (Fig. 2e,h). However, cells with Lat-A-BBS treatment still

demonstrated stiffness-dependent differential traction (Fig. 2e) with a force distribution mostly concentrated along the cell periphery (Fig. 2f). These data indicate that actin polymerization contributes to stiffness-dependent force sensitivity greatly (summarized in Fig. 2i) but not completely. Particularly, formin activity appeared to be more critical than Arp2/3 in regulating myosin-independent stiffness-force sensitivity. Together, these traction data suggest that myosin-independent stiffness-dependent differential traction is mostly actin polymerization-dependent but not completely.

Formin activity and actin polymerization are required for stiffness-dependent F-actin retrograde flow speed changes while Arp2/3 activity is partially necessary

To determine whether the reduced stiffness-dependent traction in cells with actin polymerization inhibition are associated with the actin retrograde flow, we measured the F-actin flow velocity in double-inhibited cells with CK666-BBS (Supplementary Movies 11–15), SMIFH2-BBS (Supplementary Movies 16–20), or LatA-BBS (Supplementary Movies 21–25) using qFSM. Cells treated with CK666-BBS showed a decrease in actin flow speed with stiffness in small-to-intermediate stiffness, *i.e.*, 0.6 kPa to 2.6 kPa, then the trend became constant in higher stiffness, *i.e.*, 6 kPa to 12.7 kPa (Fig. 3a). This trend is similar to the flow trend shown by myosin-inhibited cells (Fig. 1g) with a slightly smaller flow speed with no significance (Fig. 3g), representing that the traction trend by cells with Arp2/3 and myosin inhibitions is flow-dependent. Most of the high flow regime was detected at the periphery of the cell (Fig. 3b) as in myosin-inhibited cells. In contrast, the double-inhibition against myosin and formin, *i.e.*, with SMIFH 2-BBS treatment, diminished most of the flow and left only small stiffness-dependency at the low stiffness regime (Fig. 3c). Further, cells with LatA-BBS treatment have shown a constant flow speed constant regardless of the across all stiffness (Fig. 3e,f,h). As such, overall flow speed was reduced in cells with SMIFH2-BBS and LatA-BBS treatment compared to CK666-BBS-treated cells (Fig. 3h). This gradual reduction in stiffness-dependence of the actin flow speed, i.e., from BBS-only to CK666-BBS to SMIFH2-BBS to LatA-BBS (Fig. 3i), is consistent with the gradual reduction in differential traction observed (Fig. 2i). Together, these flow results suggest that the reduced stiffness-dependent force transmission is highly associated with the actin's contribution to the retrograde flow, but it requires further explanation, *e.g.*, from a model.

Traditional molecular-clutch model assuming rigid actin flow alone cannot explain Arp2/3-dependent, myosin-independent flow-traction behaviors

Stiffness-dependent traction transmission has been explained by a molecular clutch model where traction is transmitted to the ECM by a dynamic clutch between integrin-based adhesion complex against a flowing F-actin [15,18,19]. In the model, a higher traction is transmitted against stiffer ECM because the traction develops in a faster rate if the clutch engagement is stable[18]. Another contributing component has been a myosin II that pulls F-actin with a muscle-like behavior, *i.e.*, an inverse relationship between the flow velocity and the force in the fiber[58–60]. For example, the same amount of the force pulls the

stiffer ECM with less deformation. A slower deformation rate v_{myo} against a stiffer ECM gives rise to a higher force F_{myo} according to the force-velocity relationship (*e.g.*, a linearized inverse relationship such as in $F_{myo} = F_{stall}\left(1 - v_{myo}/v_o\right)$). However, this model has relied solely on the myosin for a force generator and thus was not able to explain our traction data (Figs. 1 and 2) with myosin inhibition.

To explain myosin-independent, stiffness-dependent traction trend, we added actin polymerization-powered retrograde flow velocity to the model (Fig. 4a and Supplementary Note 2). The polymerizing actin can create not only edge protrusion but the retrograde flow by being pushed back by the membrane[19,59]. When both edge protrusion speed and actin flow speed were quantified from the individual cells, we found that the retrograde flow speed was proportional with cell protrusion speed in response to gel stiffness (Supplementary Fig. 3). This demonstrates that actin polymerization gives a balanced contribution to both membrane protrusion and actin retrograde flow. Thus, for the model, we assumed that the actin polymerization-powered flow velocity v_{actin} is proportional with the actin polymerization rate and ignored the edge movement. Importantly, *in-vitro* experiments[61,62] and physics models[63,64] have found that polymerizing actin also exhibits an inverse relationship between the protrusion force and the polymerization rate. Accordingly, we modeled actin-polymerization-powered retrograde velocity v_{actin} as an inverse function (but linearized) of a force (Fig. 4a), as done similarly for v_{myo}.

To simulate the myosin-inhibited, stiffness-dependent traction response, we forced v_{myo} to be zero, which left only v_{actin} alive, while both velocities were alive for the simulation of WT cell traction behavior. As suggested from in-vitro measurements[65–67], we assumed the stall force for actin polymerization is near one-third of the stall force by myosin. This simulation was able to recapitulate the stiffness-dependent traction trend (Fig. 1a,c) by showing overall diminished force magnitude by BBS-treated cells compared to those by WT cells but a still differentially increasing traction trend in a stiffness-dependent manner (Fig. 4b). Similarly, the same simulation resulted in the inverse trend of actin flow speed as a function of the stiffness for both WT and BBS-treated cases with 3-fold lower speed in BBS-treated cell cases than the one for WT cell cases (Fig. 4c), recapitulating the experimental findings (Fig. 1e,g). This could be understood on the framework of the traditional molecular clutch model[18] except for the added v_{actin}. Briefly, the F-actin network on a soft substrate flows faster because the tension develops slower owing to the substrate compliance, which allows still a large velocity according to the force-velocity relationship ($F_{actin} = F_{stall}\left(1 - v_{actin}/v_o\right)$). But due to limited lifetime of the clutch linking both F-actin and the ECM, the substrate deforms finitely, thus transmitting still small traction, (Supplementary Fig. 4, *left*). On a stiffer substrate, the tension develops at a faster rate, which results in smaller velocity from the force-velocity relationship, thus resulting in more frequent clutch unbinding but still higher traction (Supplementary Fig. 4, *right*).

Next, we attempted to predict the traction-and-flow behaviors exhibited by cells with Arp2/3 and myosin inhibitions. Our experimental data showed that the traction magnitude in myosin-inhibited cells was nearly 4 times larger than Arp2/3-myosin-inhibited cells (Fig. 2i, *red vs. green*) while the flow speed

differed by only ~ 20% (Fig. 3i, *red vs. green*). To recapitulate this seemingly excessive difference, we simulated our model with a lower stall force (F_{stall}) for CK666-BBS case in the actin's force-velocity relationship (Fig. 4d), with a rationale that the polymerizing actin could bear much smaller force without Arp2/3 than one with it. This input indeed lowered the traction by 4-fold compared to the BBS-only condition setting (Fig. 4e, *orange vs. blue*). However, the simulation led to an actin flow speed too much lower than that from BBS-only setting (Fig. 4f, *orange vs. blue*). The reason why the flow reaches near zero was because we didn't allow the adhesion unclutching by elevating k_{off} rate constant. To allow more unclutching events, we lowered k_{off} value in the model, and this model was able to simulate high-enough actin flow speed compared to BBS-only model (Fig. 4f, *orange vs. purple*). However, this change led to further reduction in traction as well (Fig. 4e, *orange vs. purple*), resulting in too low traction magnitude overall. Together, the traditional clutch model partially explains myosin-independent, stiffness-dependent differential traction but contains a limit when it comes to contributions from actin nucleators.

Considering actin elasticity can explain the mechano-sensitive roles of actin nucleators.

We figured that the main problem of the traditional model was that the F-actin in the model was assumed to be a perfectly rigid body and its movement was determined solely by the force-velocity relationship not by the force-balance and constitutive equation, *e.g.*, Hooke's law. In that setting, if the actin-clutch binding-unbinding dynamics is similar, it becomes difficult for the flowing actin to transmit considerably different force levels from a similar level flow velocities. To overcome this difficulty, we considered the F-actin's own elasticity for the model. F-actin, in multi-scales, has its own viscoelasticity[68,69]. Furthermore, from an in-vitro experiment, the elasticity of a purified actin gel has been reported to become larger with Arp2/3 addition[70]. Mechanically, the softer F-actin becomes, the less force it could transmit with the same displacement. To test this idea, we modeled the polymerizing actin as a viscoelastic continuum material (Fig. 5a). At the polymerizing tip, actin grows by addition of discrete elastic actin unit with length *L*, of which the viscoelasticity is determined in mesoscale, i.e., by an integrative effect from the 3D actin architecture and molecular interactions (Fig. 5b) (see Supplementary Note 3 for details). The addition of new actin unit compresses the 1D actin network which is bounded by individual adhesion clutches. The compressed elastic force is transmitted to the clutches, which is again transmitted to the elastic substrate as a traction force, F_{ECM} (Fig. 5c). As more F-actin units are added, the more compressive force progressively loads either slowly or quickly depending on the substrate stiffness or the actin elasticity. The addition of the actin unit is controlled by the level of compression of spring, i.e., if the actin springs are densely packed, less actin units can be added (Eq. $N_{new} = N_{nmax} - \frac{N_{nmax}}{F_{s,actin} * F_{c,max}}$). Upon release of clutch from the ECM due to high-force and slip-bond adhesion kinetics, the compressed actin units relax by expansion, creating a quick retrograde flow, dampened by actin viscosity (Fig. 5c, a *damper with a coefficient η*).

On a soft substrate, with soft actin, individual actin units can be added quickly due to easy deformability of soft substrate, leading to fast actin flow but smaller traction due to slower force development (Supplementary Fig. 5a). With stiff actin, the retrograde flow can be further accelerated given small

resistance from low k_{sub}, resulting in medium level of traction (Supplementary Fig. 5b). On a stiff substrate, with high k_{actin}, the force develops fast due to high k_{sub}, which allows a large traction overall but slows the actin flow by limiting the addition of the actin units and triggers unclutching via raising off-rate of the adhesion (Supplementary Fig. 5d). If the actin is softer (low k_{actin}), *e.g.*, by inhibition of Arp2/3 activity, even on the substrate with high k_{sub}, the force develops much slower than a model with high k_{actin} even if actin addition rate is similar (Supplementary Fig. 5c). At the same time, due to lower k_{actin}, the same number of the actin units leads to smaller displacement thus slower flow speed (Supplementary Fig. 5c).

Via changing values of only the actin elasticity k_{actin}, from k_{actin} = 11000 for BBS to k_{actin} = 1500 for CK666-BBS case, the new model was able to recapitulate the experimental traction and flow data between BBS-treated vs. BBS-CK666-treated cells, *i.e.*, by exhibiting ~ 4-fold difference in traction (Fig. 5c) but ~ 20% difference in actin flow speed (Fig. 5d). This suggests that the consideration of Arp2/3 to F-actin elasticity is important for the force-sensitivity to the ECM stiffness. We also sought to simulate the results with SMIFH2-BBS treatment and LatA-BBS treatment using k_{actin} as the main variable. Interestingly, by further lowering k_{actin} with slight increase in viscosity , the model was able to recapitulate the stiffness-dependent differential tractions (Fig. 5e) with much less (for SMIFH2-BBS-mimicking simulation with k_{actin} = 1150 and = 1.08) or near-flat (for LatA-BBS-mimicking simulation with k_{actin} = 1000 and = 0.8) actin flow speed in response to the ECM stiffness (Fig. 5f). Together, our new model simulation results suggest that actin elasticity plays an important mechano-sensitive role independently of myosin.

Frequency of actin flow speed increases with ECM stiffness as the new model predicts.

Our model predicts that during clutch engagement, the F-actin unit addition induces minimal F-actin displacement while the unclutching event leads to rapid expansion of the compressed actin network, thus exhibiting high flow speed. Accordingly, cycles of clutching and unclutching could create fluctuations in F-actin flow speed. As the force builds up faster on a stiff ECM, the potential fluctuation could become also faster. Indeed, our model simulation with the same off-rate of the clutch predicted that the stiffer the substrate is, the more often the clutch is released and thus allows more frequent actin flow speed fluctuations (Fig. 6a). Power spectrum analysis of the frequencies of the simulated time series has confirmed this stiffness-dependent flow speed frequency (Fig. 6b,c). To identify whether this flow characteristics is present in fibroblasts, we analyzed the actin flow field of BBS-treated cells by sampling from finite-sized windows, 2 μm by 2 μm, along the cell perimeter of a cell area. An example flow velocity in a window of a cell on a soft (0.6 kPa) substrate (Fig. 6d) was high overall (Fig. 6e) but the transformation into a frequency domain showed that it exhibited a low frequency spectrum overall with majority of power in a low (0.005–0.01 Hz) frequency regime (Fig. 6f). In contrast, a small flow vector found in a cell on a stiff (12.7kPa) substrate exhibited more fluctuation compared to the overall magnitude (Fig. 6g,h). Analyzing the frequency spectrum showed significant power not only in a low frequency regime but also in a high frequency (0.04–0.08 Hz) regime (Fig. 6i). Indeed, the average

frequencies collecting from several cells and hundreds of windows showed an increase as a function of the stiffness (Fig. 6j, $p < 8 \cdot 10^{-6}$ from power-law fit). Unlike the simulation, normalized power spectrums of all windows appeared similar among all stiffness conditions (Fig. 6k). However, there were higher powers in cells on stiffer substrates in the high frequency regime, e.g., 0.06–0.08 Hz (Fig. 6k, inset), which led to the difference observed in the average frequency (Fig. 6j). Together, this quantification helps validate the actin elasticity-based molecular clutch model for actin-based rigidity sensing.

Outlook

Here we provide a stiffness-sensing mechanism for adherent cells that relies not on myosin contractility but on actin polymerization. Our model suggests that actin nucleators control the sensitivity for stiffness-dependent differential force transmission by modulating the elasticity of the polymerizing actin. Our data demonstrate that the retrograde flow, which still exists in the absence of myosin activity via actin polymerization[29,48,71], is able to induce the stiffness-dependent differential transmission. While actin polymerization has been well established for its relationship between the pushing force *vs.* extension velocity[62,63,72], to the best of our knowledge, such actin-polymerization-based force has not been shown to be stiffness-dependent[61,67]. Our work suggests that only after combining the actin polymerization-generated flow with the clutch dynamics, the stiffness-dependent differential force can be revealed.

Our results show that actin flow decreases upon inhibition of myosin and Arp2/3, which is consistent with those reported with a neuronal cell [71]. In that study, upon Arp2/3 inhibition, an even faster actin flow has been reported than one by control WT cells[71]. Only after additional inhibition of myosin the flow speed became much smaller than WT cells[71]. Their results imply that Arp2/3-mediated branched actin meshwork resists against myosin-generated F-actin flow, without which the flow can be even more accelerated. Our data suggest that if myosin activity is inhibited, Arp2/3 actively participates in retrograde flow generation, without which actin flow is reduced. We speculate that the reason for accelerated flow with Arp2/3-only inhibition is Arp2/3's involvement with nascent adhesions potentially through vinculin, providing friction against flowing actin[73–75]. Considering Arp2/3-adhesion coupling, it is possible that the reduced traction in cells with CK666-BBS is in part attributed to weaker adhesivity triggered by Arp2/3 inhibition, in addition to less actin elasticity we presented here.

Our data demonstrate that formin endows more mechano-sensitivity to cell-ECM adhesions than Arp2/3 across all stiffness. This result could be recapitulated by lowering the elasticity of the actin in the case of formin inhibition compared to Arp2/3 inhibition in the new model. Why and how formin contributes to F-actin elasticity more strongly than Arp2/3 is not clearly understood. One idea is that formin contributes to the actin elasticity by controlling the average filament length. Formin inhibition by SMIFH2 has shown to decrease the length of long actin filaments[76–78] whereas branching by Arp2/3 decreases the average actin length[79]. An *in-vitro* reconstitution study using purified actin and a capping protein gelsolin has shown that the longer the actin filament is, the stiffer the actin gel becomes[68]. At the first look, actin stiffening by filament lengthening appears counterintuitive. A traditional bio-polymer model, also known

as an affine model, predicts that the distance between crosslinks negatively controls the elastic modulus[80]. A similar model combined with cell membrane predicts that long actin filaments cannot withstand a large force because they bend under the force whereas shorter filaments can transmit forces much more efficiently[81]. These models thereby might not be able to explain the proportional relationship between the actin length and the actin elasticity. As an alternative, the length-dependent actin stiffening has been explained by a model of rigid polymers connected by flexible crosslinks[68,82,83]. In this model, a longer filament can accommodate the greater number of flexible crosslinks along its length, which allows the gel to withstand a larger load[68]. A further developed mathematical model, referred to as 'hairy rod model', predicts that an increase in filament length results in not only stiffening but also temporary softening when the length increases beyond twenty times of the filament radius[84]. Together, formin might contribute to the actin elasticity and thereby the mechanosensitivity by increasing the average filament length but up to small length scale.

It has been known that fibroblasts adapt their own elasticity to the ECM stiffness[85]. The actin elasticity, which takes an important part in the cell's cortex elasticity, is governed by not only passive crosslinkers that include Arp2/3 and formin[86] but also active force-generating crosslinkers like myosin[44]. *In vitro* reconstituted systems[87,88] and *in vivo*[89], branched actin networks have been shown to be mechanosensitive i.e. increase in branching density with increasing load. Whether Arp2/3 or formin regulation in response to the ECM stiffness affects the actin elasticity, to the best of our knowledge, has remained to be investigated. However, our model, which has used a constant actin elasticity for various ECM stiffness for a given perturbation condition, was able to reproduce the stiffness-dependent differential traction. This result implies that the clutch dynamics, powered by actin polymerization alone, could allow cells to be 'felt' stiffer by transmitting more traction even with the same actin elasticity. Thus, the cell elasticity adaptation to the ECM mechanics could be not only by actin crosslinkers but also by the clutch dynamics by both actin polymerization and myosin contractility.

Our actin elasticity-based molecular clutch model provides possible explanation for more frequent F-actin flow speed fluctuation coupled to higher substrate rigidity. The stiffness-dependent edge contraction have been reported previously in mouse embryonic fibroblasts, which has been also dependent on activities of myosin, cofilin and Rac1[90]. We believe that the reason why we observe the stiffness-dependent flow speed fluctuation is owing to a large data sampling followed by a detailed frequency analysis. Together, our simulation and experimental results suggest that the actin's elastic compression during adhesion clutch and release upon unclutching could be an important factor inducing myosin-independent flow-fluctuation.

Lastly, actin polymerization is highly coupled with the formation of nascent adhesions[91–93]. Thus, it is possible that differential force transmission in response to different stiffness is sensed at the nascent adhesion level[39]. How different early adhesion molecules are involved in this actin-based mechanosensing would be an interesting direction to further investigate.

Materials and methods

Cell culture and reagents

NIH 3T3 fibroblasts stably expressing mRuby-Paxillin, generous gift from Dr. Mark H. Ginsberg (University of California, San Diego), were cultured in Dulbecco's Modified Eagle Medium with phenol red, glutamine. 4.5 g/L D-Glucose, L-Glutamine, and Sodium Pyruvate (Corning Incorporated, Corning, NY, USA 10-013-CV) supplemented with 10% fetal bovine serum (FBS; Gibco/Invitrogen, Grand Island, NY, USA; 26140079), 1% penicillin-streptomycin (Gibco/Invitrogen, Grand Island, NY, USA; 15140122) and 1% nonessential amino acids (NEAA; Gibco/Invitrogen, Grand Island, NY, USA; 11140050) in 5% CO_2, 37 ºC condition. SNAP-actin-expressing 3T3 fibroblasts [94], a generous gift from Dr. Martin Schwartz (Yale University, New Haven, CT, USA), were cultured in DMEM (Corning Incorporated, Corning, NY, USA; 10-013-CV) with phenol red, glutamine. 4.5 g/L D-Glucose, L-Glutamine, and Sodium Pyruvate, 10% FBS (FBS; Gibco/Invitrogen, Grand Island, NY, USA; 26140079), 1% penicillin-streptomycin (Gibco/Invitrogen, Grand Island, NY, USA; 15140122) and 1% NEAA (NEAA; Gibco/Invitrogen, Grand Island, NY, USA; 11140050) and 250 µg/mL Geneticin (G418 sulfate; Gibco/Invitrogen, Grand Island, NY, USA; 10131035) in 5% CO_2 at 37 ºC. To inhibit myosin activity, (-)-Blebbistatin (13013) was purchased from Cayman Chemicals (Ann Arbor, MI, USA). Formin activity inhibitor SMIFH2 (340316-62-3) was purchased from Abcam (Cambridge, United Kingdom, USA). Arp2/3 Complex Inhibitor I, CK-666 (442633-00-3) and Arp2/3 Complex Inhibitor I, Inactive Control, CK-689 (170930-46-8) were purchased from Calbiochem/MilliporeSigma (Burlington, MA, USA). To disrupt actin network, Latrunculin A (76343-93-6) was obtained from Cayman chemicals (Ann Arbor, MI, USA).

Soft substrate preparation and stiffness characterization

High-refractive index, soft silicone gels (Q-gel, CHT, Richmond, VA, USA) of different stiffness were fabricated as previously described[95]. Briefly, the gel substrates of five different stiffness, i.e., 0.6, 1.3, 2.7, 6 and 12.7 kPa, were made by thorough mixing of Q-gel 920-part A and B at ratio 1:1, 1:1.1, 1:.1.2, 1:1.5 and 1:2 respectively. The elastic modulus was measured by measuring the shear storage moduli (G') of the gel at each mixing ratio using a DHR-2 hybrid rheometer (TA Instruments, New Castle, DE, USA). As the Q-gel was very soft and sticky, thus hard to handle, we started to measure the gel's storage modulus from its pre-cured state on the 40 mm stainless steel Peltier parallel plate stage by a time-sweep test for 10 hours with 0.63 rad/s oscillation amplitude. The gel was cured to its final stiffness during the test. The metal parallel plate was heated to 80 ℃ to match the curing temperature of the gels, the gap height was set at 20 µm to accommodate an initially less viscous gel, and strain was set to 1% to stay within the linear viscoelastic regime. This testing was performed via a time sweep program in TRIOS software.

For TFM substrate fabrication, 300 µl of the Q-gel920 A/B mixture was spin-coated on a 35-mm glass-bottom dish with a No. 1.0, 14 mm-diameter circular cover glass (MatTek, Ashland, MA, USA) at 1000 RPM for 30 sec min, followed by curing at 80°C for 2 hrs. A slower spinning speed, i.e., than the original

method (3000 RPM) in [95], was chosen to increase the gel thickness and to avoid the cells from sensing the rigidness of the glass bottom. The gel thickness was measured by profilometer to be ~ 45 μm in average. To functionalize the gel surface, (3-aminopropyl) triethoxysilane (APTES, Sigma-Aldrich, St. Louis, MO, USA; 440140) was treated on the coated gel. As fiducial markers for gel deformation visualization, 40-nm carboxylated far-red fluorescent beads (Invitrogen/Thermo Fisher scientific, Waltham, MA, USA; F8789) with a density of 1 bead /μm^2 (excitation/emission 660/680 nm, Invitrogen, Waltham, MA) were covalently bonded on the gel surface using 1-Ethyl-3-(3-dimethylaminopropyl) carbodiimide (EDC, Sigma-Aldrich, St. Louis, MO, USA; 39391).

Traction microscopy imaging

For traction force microscopy experiments, the silicone gel on a glass-bottom dish (MatTek, Ashland, MA, USA) was coated with 10 μg/ml fibronectin for 30min at RT. 3T3 fibroblasts expressing mRuby-Paxillin were plated on the fibronectin-coated gel substrates. 4 hrs after seeding, the beads and the paxillin were imaged under total internal reflection fluorescence (TIRF) microscope (optoTIRF, CAIRN Research, Faversham ME13 8UP, UK) housed in Nikon Ti-S microscope (Nikon Instruments, Melville, NY, USA) at a 60x TIRF objective. The microscope stage was equipped with an H301 stage-top incubator chamber and UNO controller (Okolab USA Inc, San Bruno, CA, USA) to maintain cells at 5% CO2 and 37°C in a humid environment. The single-shot live cell imaging was performed in phenol-red-free DMEM (Gibco/Invitrogen, Grand Island, NY, USA; 31053028) supplemented with 10% fetal bovine serum (FBS; Gibco/Invitrogen, Grand Island, NY; 26140079), 1% penicillin-streptomycin (Gibco/Invitrogen, Grand Island, NY, USA; 15140122) and 1% nonessential amino acids (NEAA; Gibco/Invitrogen, Grand Island, NY, USA; 11140050). The cells were kept in focus using CRISP autofocus unit (ASI Applied Scientific Instrumentation, Eugene, OR, USA). The far-red fluorescent beads signal and mRuby paxillin signal were imaged at the same focal plane, i.e., on top of the gel, with 642nm and 587nm lasers, respectively. The images were captured with a Hamamatsu ORCA-flash 4.0 LT plus sCMOS camera (Hamamatsu Corporation, Bridgewater. NJ, USA) and controlled with MetaMorph imaging software (Molecular Devices, Downington, PA, USA). The bead images with relaxed gel were obtained after removing the cells using 0.5 ml of 10% bleach.

Perturbations using small-molecular inhibitors

For TFM experiments, for myosin contractility inhibition, 20 μM of blebbistatin (BBS) was applied to cells for 1 hr after 3 hrs of cell seeding on the gel. The BBS concentration and sequence of cell seeding and treatment were chosen to inhibit most myosin II ATPase activity with minimum toxicity while ensuring cell adhesion (Supplementary Note 1). For inhibition of Arp2/3 complex, 100 μM CK666 was applied to cells in addition to BBS for 1 hr after 3 hrs of cell seeding on the gel. To inhibit formin FH2 domain activity, 20 μM SMIFH2 were used, in addition to BBS, for 1 hr after 3 hrs of cell seeding on the gel. As a negative control of CK666 treatment, 100 μM of CK689, inactive structural analogue, was applied to cells for an imaging experiment. Inhibition of actin polymerization itself was done using 1μM latrunculin-A along with

20 μM BBS. The same concentrations of inhibitors were used for the actin speckle flow experiments. The inhibitors were applied 30 mins after cell seeding to the gel substrate to ensure imaging of cell protrusion and lamellipodia.

Traction reconstruction

From a pair of bead images acquired in the presence and absence of cells, traction was reconstructed using our MATLAB-based TFMPackage software[40,41]. Briefly, the displacement field was calculated by a cross-correlation-based particle tracking velocimetry with retracking (cPTVR) method that is able to track large, local displacement[38]. The force reconstruction was performed using Fast Boundary Element Method (FastBEM) with L_2-norm-based regularization where a regularization parameter was chosen based on L-curve, L-corner method. Acquired traction fields were interpolated over the original microscopic image area and quantified for an average traction over a 2 μm-thick perimeter band area from a cell segmentation captured from corresponding mRuby-paxillin channel images.

Actin fluorescence speckle imaging

For time-lapse live-cell imaging of actin speckles, SNAP actin-expressing 3T3 fibroblasts were labeled by culture in a 24-well culture dish up to 70% confluency followed by incubation with 0.5 μM SNAP-Cell 647-SiR (New England Biolabs, Ipswich, MA, USA; S9102S) at 37°C for 30 min. Cells were then washed thoroughly with the DMEM phenol-red-free media every 30 min for 2 hrs. They were incubated at 37°C for 30 min after every wash. SNAP-Cell 647-SiR labelled cells were then seeded on fibronectin-coated silicone gel on top of glass-bottom dishes (#1, 14-mm-diameter glass coverslip, 35-mm dish: MatTek, Ashland, MA, USA). Actin-speckle imaging was performed after 45 min-1 hr of cell seeding. Actin speckles were imaged under a spinning-disk confocal microscopy, a Nikon Ti-S microscope equipped with Yokogawa spinning disk head (CSUX1), stage-top based incubation chamber system (OkoLab, Ambridge, PA, USA), XY motorized stage with linear encoders (ASI Applied Scientific Instrumentation, Eugene, OR, USA), a focus-drift-compensation system (CRISP with 780 nm LED), and a high-resolution, high-frame-rate camera (ORCA-Flash LT sCMOS). A laser line with 642nm wavelength was used for exciting SNAP-actin-SiR647, and cells were imaged under a 100x objective for 3 mins with a time interval of 6 seconds (64.5 nm per pixel, NA = 1.4, 16-bit images).

Actin retrograde flow quantification from speckle images

Quantification of time-lapse actin speckle movies was performed using quantitative fluorescence speckle microscopy (qFSM) software in MATLAB (MathWorks)[48,96]. First, images acquired at 6 frames per minute were calibrated using noise model calibration. Cell masks were generated using manual thresholding. Speckles were detected by setting the alpha value for statistical selection of speckles (0.05) with maximum iteration at 3. Flow tracking was performed on 1 to 31 frames with a 2-frame integration

window, 1-frame step size, template size range 17–35 pixels, maximum flow speed 10 pixels/frame. As additional settings, mask edge erosion width was set at 5 pixels, and the relative distance for filtering vector outlier in respect to local neighborhood was set to 1. Speckles were tracked by performing a hierarchical tracking using nearest neighbor flow with search radius of 3 pixels and correlation length of 33 pixels. Flow analysis was performed using speckle tracking as the flow process to analyze by time averaging for 3 number of frames, correlation length of 33 pixels and grid size width of 11 pixels. For SMIFH2 and latrunculin-A actin-speckles time-lapse images, PIV was used for flow quantification instead of particle tracking because not many individual speckles were detectable using Gaussian fit-based detection. A potential stage drift was checked for each movie by a user and by a software. Actin flow speed was quantified in the five different layers of the cell from the cell edge with 2 μm in thickness for each layer.

Statistical analysis

Comparison of normalized traction (Fig. 2g) and normalized flow speed (Fig. 3g) between blebbistatin (BBS) and CK666-BBS treated cells was done using Mann-Whitney U nonparametric test because most of the data were non-Gaussian which was tested by Kolmogorov-Smirnov test. Comparison of normalized traction (Fig. 2h) and normalized flow speed (Fig. 3h) among CK666-BBS, SMIFH2-BBS and Lat-A-BBS treated cells was done using Kruskal-Wallis ANOVA and Dunn's post-hoc analysis.

Actin-elasticity-based, actin-polymerization-powered molecular clutch model and code availability

The parameters and implementations of computation model for molecular clutch is described in detail in the Supplementary Note 3. A set of MATLAB codes and functions used for the modeling is available upon request to sjhan@mtu.edu.

Declarations

Acknowledgements

We thank Dr. Martin A. Schwartz (Yale University) for sending us SNAP-actin-expressing 3T3s. We appreciate practical advice from Dr. Tristan Driscoll (University of Florida) about the fluorescence speckle microscopy experiment. We also thank Dr. Pere Roca-Cusachs (Institute for Bioengineering of Catalonia and University of Barcelona) for providing us with their myosin-powered molecular clutch model. We are also grateful to Dr. Mark H. Ginsberg and Dr. Ho-sup Lee (UCSD) for the 3T3 fibroblast cells stably expressing mRuby-Paxillin as a kind gift.

References

1. Engler, A. J. *et al.* Myotubes differentiate optimally on substrates with tissue-like stiffness: pathological implications for soft or stiff microenvironments. *The Journal of cell biology* **166**, 877-887 (2004).
2. Engler, A. J., Richert, L., Wong, J. Y., Picart, C. & Discher, D. E. Surface probe measurements of the elasticity of sectioned tissue, thin gels and polyelectrolyte multilayer films: correlations between substrate stiffness and cell adhesion. *Surface science* **570**, 142-154 (2004).
3. Engler, A. J., Sen, S., Sweeney, H. L. & Discher, D. E. Matrix elasticity directs stem cell lineage specification. *Cell* **126**, 677-689 (2006).
4. Mih, J. D., Marinkovic, A., Liu, F., Sharif, A. S. & Tschumperlin, D. J. Matrix stiffness reverses the effect of actomyosin tension on cell proliferation. *Journal of cell science* **125**, 5974-5983 (2012).
5. Ulrich, T. A., de Juan Pardo, E. M. & Kumar, S. The mechanical rigidity of the extracellular matrix regulates the structure, motility, and proliferation of glioma cells. *Cancer research* **69**, 4167-4174 (2009).
6. Lo, C.-M., Wang, H.-B., Dembo, M. & Wang, Y.-l. Cell movement is guided by the rigidity of the substrate. *Biophysical journal* **79**, 144-152 (2000).
7. Hoffman, B. D., Grashoff, C. & Schwartz, M. A. Dynamic molecular processes mediate cellular mechanotransduction. *Nature* **475**, 316-323 (2011).
8. Sun, Z., Guo, S. S. & Fässler, R. Integrin-mediated mechanotransduction. *Journal of Cell Biology* **215**, 445-456 (2016).
9. Geiger, B., Spatz, J. P. & Bershadsky, A. D. Environmental sensing through focal adhesions. *Nature reviews Molecular cell biology* **10**, 21-33 (2009).
10. Austen, K. *et al.* Extracellular rigidity sensing by talin isoform-specific mechanical linkages. *Nature cell biology* **17**, 1597-1606 (2015).
11. Han, S. J., Bielawski, K. S., Ting, L. H., Rodriguez, M. L. & Sniadecki, N. J. Decoupling substrate stiffness, spread area, and micropost density: a close spatial relationship between traction forces and focal adhesions. *Biophysical journal* **103**, 640-648 (2012).
12. Ghibaudo, M. *et al.* Traction forces and rigidity sensing regulate cell functions. *Soft Matter* **4**, 1836-1843 (2008).
13. Oakes, P. W., Banerjee, S., Marchetti, M. C. & Gardel, M. L. Geometry regulates traction stresses in adherent cells. *Biophysical journal* **107**, 825-833 (2014).
14. Guo, W.-h., Frey, M. T., Burnham, N. A. & Wang, Y.-l. Substrate rigidity regulates the formation and maintenance of tissues. *Biophysical journal* **90**, 2213-2220 (2006).
15. Elosegui-Artola, A. *et al.* Rigidity sensing and adaptation through regulation of integrin types. *Nature materials* **13**, 631-637 (2014).
16. Plotnikov, S. V., Pasapera, A. M., Sabass, B. & Waterman, C. M. Force fluctuations within focal adhesions mediate ECM-rigidity sensing to guide directed cell migration. *Cell* **151**, 1513-1527 (2012).

17. Bangasser, B. L. & Odde, D. J. Master equation-based analysis of a motor-clutch model for cell traction force. *Cellular and molecular bioengineering* **6**, 449-459 (2013).
18. Elosegui-Artola, A. *et al.* Mechanical regulation of a molecular clutch defines force transmission and transduction in response to matrix rigidity. *Nature cell biology* **18**, 540-548 (2016).
19. Chan, C. E. & Odde, D. J. Traction dynamics of filopodia on compliant substrates. *Science* **322**, 1687-1691 (2008).
20. Hoon, J. L., Tan, M. H. & Koh, C.-G. The regulation of cellular responses to mechanical cues by Rho GTPases. *Cells* **5**, 17 (2016).
21. Guilluy, C. *et al.* The Rho GEFs LARG and GEF-H1 regulate the mechanical response to force on integrins. *Nature cell biology* **13**, 722-727 (2011).
22. Totsukawa, G. *et al.* Distinct roles of MLCK and ROCK in the regulation of membrane protrusions and focal adhesion dynamics during cell migration of fibroblasts. *The Journal of cell biology* **164**, 427-439 (2004).
23. Vicente-Manzanares, M., Ma, X., Adelstein, R. S. & Horwitz, A. R. Non-muscle myosin II takes centre stage in cell adhesion and migration. *Nature reviews Molecular cell biology* **10**, 778-790 (2009).
24. Kanchanawong, P. *et al.* Nanoscale architecture of integrin-based cell adhesions. *Nature* **468**, 580-584 (2010).
25. Choquet, D., Felsenfeld, D. P. & Sheetz, M. P. Extracellular matrix rigidity causes strengthening of integrin–cytoskeleton linkages. *Cell* **88**, 39-48 (1997).
26. Schiller, H. B. & Fässler, R. Mechanosensitivity and compositional dynamics of cell–matrix adhesions. *EMBO reports* **14**, 509-519 (2013).
27. Ji, L., Lim, J. & Danuser, G. Fluctuations of intracellular forces during cell protrusion. *Nature cell biology* **10**, 1393-1400 (2008).
28. Beningo, K. A., Hamao, K., Dembo, M., Wang, Y.-l. & Hosoya, H. Traction forces of fibroblasts are regulated by the Rho-dependent kinase but not by the myosin light chain kinase. *Archives of biochemistry and biophysics* **456**, 224-231 (2006).
29. Gardel, M. L. *et al.* Traction stress in focal adhesions correlates biphasically with actin retrograde flow speed. *The Journal of cell biology* **183**, 999-1005 (2008).
30. Zhou, D. W., Lee, T. T., Weng, S., Fu, J. & García, A. J. Effects of substrate stiffness and actomyosin contractility on coupling between force transmission and vinculin–paxillin recruitment at single focal adhesions. *Molecular biology of the cell* **28**, 1901-1911 (2017).
31. Oakes, P. W. *et al.* Lamellipodium is a myosin-independent mechanosensor. *Proceedings of the National Academy of Sciences* **115**, 2646-2651 (2018).
32. Wahl, A. *et al.* Biphasic mechanosensitivity of T cell receptor-mediated spreading of lymphocytes. *Proceedings of the National Academy of Sciences* **116**, 5908-5913 (2019).
33. Pollard, T. D. & Cooper, J. A. Actin, a central player in cell shape and movement. *science* **326**, 1208-1212 (2009).

34. Johnson, H. E. *et al.* F-actin bundles direct the initiation and orientation of lamellipodia through adhesion-based signaling. *Journal of Cell Biology* **208**, 443-455 (2015).
35. Mullins, R. D., Stafford, W. F. & Pollard, T. D. Structure, subunit topology, and actin-binding activity of the Arp2/3 complex from Acanthamoeba. *The Journal of cell biology* **136**, 331-343 (1997).
36. Romero, S. *et al.* formin is a processive motor that requires profilin to accelerate actin assembly and associated ATP hydrolysis. *Cell* **119**, 419-429 (2004).
37. Lee, K. *et al.* Functional hierarchy of redundant actin assembly factors revealed by fine-grained registration of intrinsic image fluctuations. *Cell systems* **1**, 37-50 (2015).
38. Haarman, S. E., Kim, S. Y., Isogai, T., Dean, K. M. & Han, S. J. Particle retracking algorithm capable of quantifying large, local matrix deformation for traction force microscopy. *PloS one* **17**, e0268614 (2022).
39. Han, S. J. *et al.* Pre-complexation of talin and vinculin without tension is required for efficient nascent adhesion maturation. *Elife* **10**, e66151 (2021).
40. Han, S. J., Oak, Y., Groisman, A. & Danuser, G. Traction microscopy to identify force modulation in subresolution adhesions. *Nature methods* **12**, 653 (2015).
41. Mittal, N. & Han, S. J. High-Resolution, Highly-Integrated Traction Force Microscopy Software. *Current protocols* **1**, e233 (2021).
42. Kovács, M., Tóth, J., Hetényi, C., Málnási-Csizmadia, A. & Sellers, J. R. Mechanism of blebbistatin inhibition of myosin II. *Journal of Biological Chemistry* **279**, 35557-35563 (2004).
43. Limouze, J., Straight, A. F., Mitchison, T. & Sellers, J. R. Specificity of blebbistatin, an inhibitor of myosin II. *Journal of Muscle Research & Cell Motility* **25**, 337-341 (2004).
44. Doss, B. L. *et al.* Cell response to substrate rigidity is regulated by active and passive cytoskeletal stress. *Proceedings of the National Academy of Sciences* **117**, 12817-12825 (2020).
45. Dumbauld, D. W. *et al.* How vinculin regulates force transmission. *Proceedings of the National Academy of Sciences* **110**, 9788-9793 (2013).
46. Mikulich, A., Kavaliauskiene, S. & Juzenas, P. Blebbistatin, a myosin inhibitor, is phototoxic to human cancer cells under exposure to blue light. *Biochimica et Biophysica Acta (BBA)-General Subjects* **1820**, 870-877 (2012).
47. Driscoll, T. P., Huang, B., Ahn, S. J., Kumar, A. & Schwartz, M. Actin Flow Dependent and Independent Force Transmission in Integrin-Mediated Adhesions. *Biophysical Journal* **116**, 123a (2019).
48. Ponti, A., Machacek, M., Gupton, S. L., Waterman-Storer, C. M. & Danuser, G. Two distinct actin networks drive the protrusion of migrating cells. *Science* **305**, 1782-1786 (2004).
49. Watanabe, N. & Mitchison, T. J. Single-molecule speckle analysis of actin filament turnover in lamellipodia. *Science* **295**, 1083-1086 (2002).
50. Qin, Z., Voorhees, J. J., Fisher, G. J. & Quan, T. Age-associated reduction of cellular spreading/mechanical force up-regulates matrix metalloproteinase-1 expression and collagen fibril fragmentation via c-Jun/AP-1 in human dermal fibroblasts. *Aging Cell* **13**, 1028-1037 (2014).

51. Krishnan, R. *et al.* Reinforcement versus fluidization in cytoskeletal mechanoresponsiveness. *PloS one* **4**, e5486 (2009).
52. Ricart, B. G., Yang, M. T., Hunter, C. A., Chen, C. S. & Hammer, D. A. Measuring traction forces of motile dendritic cells on micropost arrays. *Biophysical journal* **101**, 2620-2628 (2011).
53. Hui, K. L., Balagopalan, L., Samelson, L. E. & Upadhyaya, A. Cytoskeletal forces during signaling activation in Jurkat T-cells. *Molecular biology of the cell* **26**, 685-695 (2015).
54. Pollard, T. D. Regulation of actin filament assembly by Arp2/3 complex and formins. *Annu. Rev. Biophys. Biomol. Struct.* **36**, 451-477 (2007).
55. Nishimura, Y. *et al.* The formin inhibitor SMIFH2 inhibits members of the myosin superfamily. *Journal of cell science* **134** (2021).
56. Hu, K., Ji, L., Applegate, K. T., Danuser, G. & Waterman-Storer, C. M. Differential transmission of actin motion within focal adhesions. *Science* **315**, 111-115 (2007).
57. Fujiwara, I., Zweifel, M. E., Courtemanche, N. & Pollard, T. D. Latrunculin A accelerates actin filament depolymerization in addition to sequestering actin monomers. *Current Biology* **28**, 3183-3192. e3182 (2018).
58. Hill, A. V. The heat of shortening and the dynamic constants of muscle. *Proceedings of the Royal Society of London. Series B-Biological Sciences* **126**, 136-195 (1938).
59. Mitrossilis, D. *et al.* Single-cell response to stiffness exhibits muscle-like behavior. *Proceedings of the National Academy of Sciences* **106**, 18243-18248 (2009).
60. Han, S. J. & Sniadecki, N. J. Simulations of the contractile cycle in cell migration using a bio-chemical–mechanical model. *Computer Methods in Biomechanics and Biomedical Engineering* **14**, 459-468 (2011).
61. Marcy, Y., Prost, J., Carlier, M.-F. & Sykes, C. Forces generated during actin-based propulsion: a direct measurement by micromanipulation. *Proceedings of the National Academy of Sciences* **101**, 5992-5997 (2004).
62. McGrath, J. L. *et al.* The force-velocity relationship for the actin-based motility of Listeria monocytogenes. *Current Biology* **13**, 329-332 (2003).
63. Mogilner, A. & Oster, G. Force generation by actin polymerization II: the elastic ratchet and tethered filaments. *Biophysical journal* **84**, 1591-1605 (2003).
64. Lee, K.-C. & Liu, A. J. Force-velocity relation for actin-polymerization-driven motility from Brownian dynamics simulations. *Biophysical journal* **97**, 1295-1304 (2009).
65. Norstrom, M. F., Smithback, P. A. & Rock, R. S. Unconventional processive mechanics of non-muscle myosin IIB. *Journal of Biological Chemistry* **285**, 26326-26334 (2010).
66. Hundt, N., Steffen, W., Pathan-Chhatbar, S., Taft, M. H. & Manstein, D. J. Load-dependent modulation of non-muscle myosin-2A function by tropomyosin 4.2. *Scientific reports* **6**, 1-12 (2016).
67. Footer, M. J., Kerssemakers, J. W., Theriot, J. A. & Dogterom, M. Direct measurement of force generation by actin filament polymerization using an optical trap. *Proceedings of the National*

Academy of Sciences **104**, 2181-2186 (2007).

68. Kasza, K. *et al.* Actin filament length tunes elasticity of flexibly cross-linked actin networks. *Biophysical journal* **99**, 1091-1100 (2010).
69. Janmey, P. A. *et al.* The mechanical properties of actin gels. Elastic modulus and filament motions. *Journal of Biological Chemistry* **269**, 32503-32513 (1994).
70. Pujol, T., du Roure, O., Fermigier, M. & Heuvingh, J. Impact of branching on the elasticity of actin networks. *Proceedings of the National Academy of Sciences* **109**, 10364-10369 (2012).
71. Yang, Q., Zhang, X.-F., Pollard, T. D. & Forscher, P. Arp2/3 complex–dependent actin networks constrain myosin II function in driving retrograde actin flow. *Journal of Cell Biology* **197**, 939-956 (2012).
72. Upadhyaya, A. & van Oudenaarden, A. Biomimetic systems for studying actin-based motility. *Current Biology* **13**, R734-R744 (2003).
73. Boujemaa-Paterski, R. *et al.* Talin-activated vinculin interacts with branched actin networks to initiate bundles. *Elife* **9**, e53990 (2020).
74. Beckham, Y. *et al.* Arp2/3 inhibition induces amoeboid-like protrusions in MCF10A epithelial cells by reduced cytoskeletal-membrane coupling and focal adhesion assembly. *PLoS One* **9**, e100943 (2014).
75. Isogai, T. *et al.* Direct Arp2/3-vinculin binding is essential for cell spreading, but only on compliant substrates and in 3D. *bioRxiv*, 756718 (2019).
76. Fritzsche, M., Erlenkämper, C., Moeendarbary, E., Charras, G. & Kruse, K. Actin kinetics shapes cortical network structure and mechanics. *Science advances* **2**, e1501337 (2016).
77. Bovellan, M. *et al.* Cellular control of cortical actin nucleation. *Current Biology* **24**, 1628-1635 (2014).
78. Eghiaian, F., Rigato, A. & Scheuring, S. Structural, mechanical, and dynamical variability of the actin cortex in living cells. *Biophysical journal* **108**, 1330-1340 (2015).
79. Carlsson, A. The effect of branching on the critical concentration and average filament length of actin. *Biophysical journal* **89**, 130-140 (2005).
80. MacKintosh, F., Käs, J. & Janmey, P. Elasticity of semiflexible biopolymer networks. *Physical review letters* **75**, 4425 (1995).
81. Zimmermann, J. *et al.* Actin filament elasticity and retrograde flow shape the force-velocity relation of motile cells. *Biophysical journal* **102**, 287-295 (2012).
82. Broedersz, C., Storm, C. & MacKintosh, F. Nonlinear elasticity of composite networks of stiff biopolymers with flexible linkers. *Physical review letters* **101**, 118103 (2008).
83. Broedersz, C., Storm, C. & MacKintosh, F. Effective-medium approach for stiff polymer networks with flexible cross-links. *Physical Review E* **79**, 061914 (2009).
84. Vernerey, F. J. Mechanics of transient semi-flexible networks: Soft-elasticity, stress relaxation and remodeling. *Journal of the Mechanics and Physics of Solids* **160**, 104776 (2022).

85. Solon, J., Levental, I., Sengupta, K., Georges, P. C. & Janmey, P. A. Fibroblast adaptation and stiffness matching to soft elastic substrates. *Biophysical journal* **93**, 4453-4461 (2007).
86. Efremov, Y. M. *et al.* Distinct impact of targeted actin cytoskeleton reorganization on mechanical properties of normal and malignant cells. *Biochimica et Biophysica Acta (BBA)-Molecular Cell Research* **1853**, 3117-3125 (2015).
87. Bieling, P. *et al.* Force feedback controls motor activity and mechanical properties of self-assembling branched actin networks. *Cell* **164**, 115-127 (2016).
88. Parekh, S. H., Chaudhuri, O., Theriot, J. A. & Fletcher, D. A. Loading history determines the velocity of actin-network growth. *Nature cell biology* **7**, 1219-1223 (2005).
89. Mueller, J. *et al.* Load adaptation of lamellipodial actin networks. *Cell* **171**, 188-200. e116 (2017).
90. Giannone, G. *et al.* Periodic lamellipodial contractions correlate with rearward actin waves. *Cell* **116**, 431-443 (2004).
91. Choi, C. K. *et al.* Actin and α-actinin orchestrate the assembly and maturation of nascent adhesions in a myosin II motor-independent manner. *Nature cell biology* **10**, 1039-1050 (2008).
92. Alexandrova, A. Y. *et al.* Comparative dynamics of retrograde actin flow and focal adhesions: formation of nascent adhesions triggers transition from fast to slow flow. *PloS one* **3**, e3234 (2008).
93. Yamashiro, S. & Watanabe, N. A new link between the retrograde actin flow and focal adhesions. *The journal of biochemistry* **156**, 239-248 (2014).
94. Driscoll, T. P., Ahn, S. J., Huang, B., Kumar, A. & Schwartz, M. A. Actin flow-dependent and-independent force transmission through integrins. *Proceedings of the National Academy of Sciences* **117**, 32413-32422 (2020).
95. Gutierrez, E. *et al.* High refractive index silicone gels for simultaneous total internal reflection fluorescence and traction force microscopy of adherent cells. *PLoS One* **6**, e23807 (2011).
96. Mendoza, M. C., Besson, S. & Danuser, G. Quantitative fluorescent speckle microscopy (QFSM) to measure actin dynamics. *Current protocols in cytometry* **62**, 2.18. 11-12.18. 26 (2012).

Supplementary Movie

Supplementary Movie 23 is not available with this version

Figures

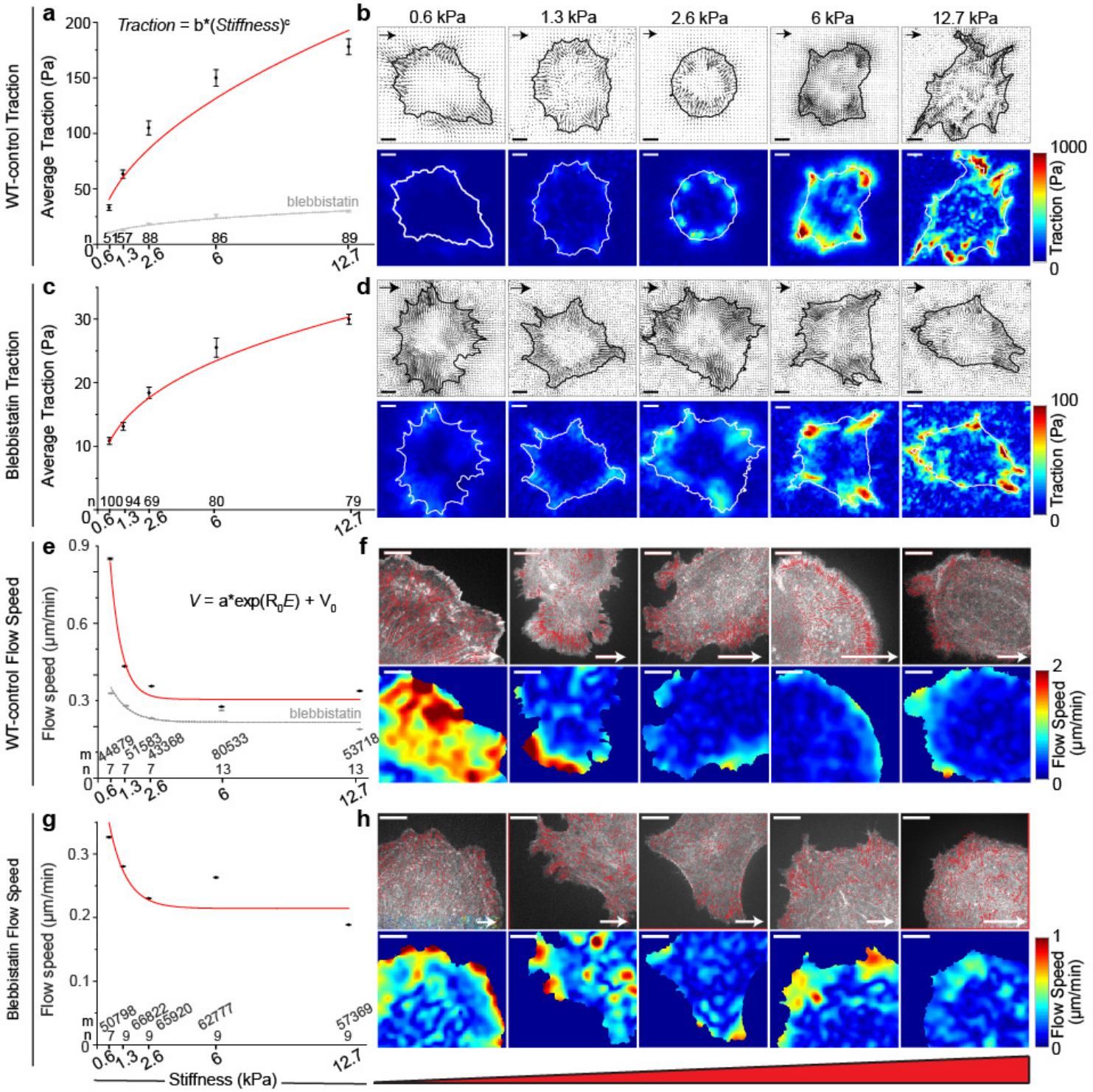

Figure 1

Stiffness-dependent differential traction is transmitted independently of myosin-II contractility in F-actin retrograde flow-dependent manner. a, Average traction integrated over 2-mm-thick cell perimeter of WT NIH 3T3 fibroblasts as a function of different gel stiffness (red). Sample sizes, *n,* are denoted on top of each stiffness value. Markers with error bars: mean ± s.e.m. **b,** Representative traction vector fields (top) and traction magnitude maps (bottom) of WT-control cells. Arrow scale: 150 Pa, 300 Pa, 500 Pa, 1500 Pa and 1500 Pa of traction for gel stiffness of 0.6 kPa, 1.3 kPa, 2.6 kPa, 6 kPa and 12.7 kPa, respectively.

Scale bar: 10 μm. **c,** Average traction integrated over cell perimeter of cells treated with 20 μM blebbistatin (BBS) as a function of a gel stiffness (grey dotted in **(a)** and red in **(c)**). **d,** Representative traction vector fields (top) and traction maps (bottom) of BBS-treated cells. Arrow scale: 50 Pa, 75 Pa, 90 Pa, 100 Pa and 150 Pa of traction for gel stiffness of 0.6 kPa, 1.3 kPa, 2.6 kPa, 6 kPa and 12.7 kPa, respectively. Power-law curve fits (Traction = b*(Stiffness)^{c}) were added in **(a)** and **(c)** (See Supplementary Table 1 for fit parameters). **e,** Average F-actin flow speed as a function of the gel stiffness of WT-control cells (red, n = 7, 7, 7, 13, 13 cells for increasing stiffness, collected from m = 44879, 51583, 43368, 80533, 53718 windows). Markers with error bars: mean ± s.e.m.. **f,** Representative interpolated flow vectors (top) and speed maps (bottom) of SNAP-actin of WT 3T3 fibroblasts on a gel with increasing stiffness. Arrow scale: 5 μm/min of actin flow. **g,** Average F-actin flow speed as a function of the gel stiffness of BBS-treated cells (grey dotted in **(e)** and red in **(g)**, n = 7, 9, 9, 9, 9 cells for increasing stiffness, m = 50798, 66822, 65920, 62777, 57369 windows). A negative exponential function (V= a*exp(R_0E) + V_0) was used for flow speed vs stiffness plots in **(e)** and **(g)** (See Supplementary Table 2 for fit parameters). **h,** Representative interpolated flow fields (top) and speed maps (bottom) of BBS-treated cells. Arrow scale: 3 μm/min of actin flow. Scale bar: 10 μm.

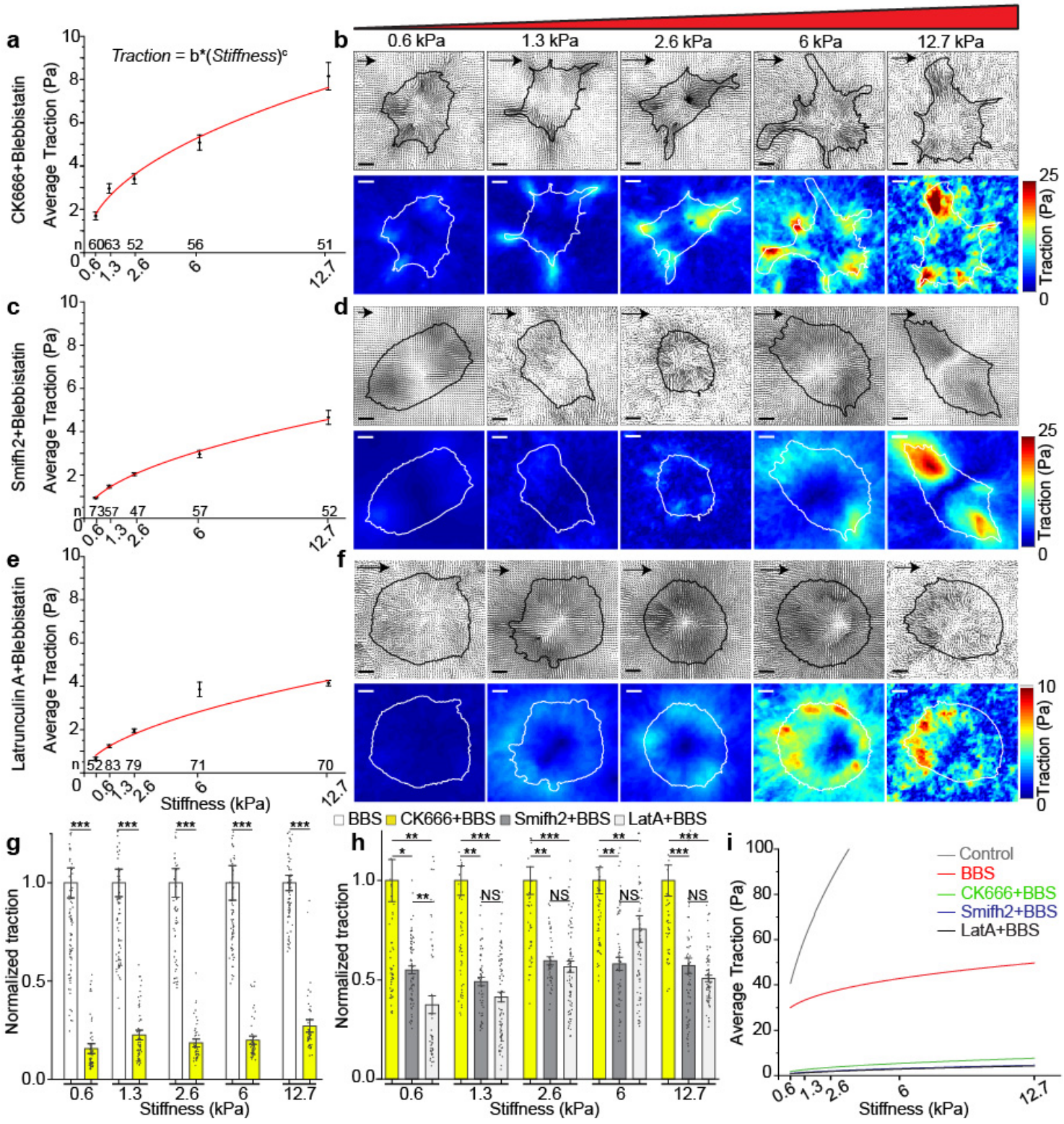

Figure 2

Myosin-independent, stiffness-dependent differential traction depends on actin polymerization mediated by Arp2/3 and formin. a, Average traction integrated over cell perimeter of cells treated with 100 μM CK666 in addition to 20 μM BBS as a function of a gel stiffness. Sample sizes, *i.e.*, the number of cells, *n,* are denoted on top of each stiffness value. Markers with error bars: mean ± s.e.m. **b,** Representative traction vector fields (top) and traction magnitude maps (bottom) of CK666- and BBS-treated cells. Arrow

scale: 10 Pa, 30 Pa, 40 Pa, 50 Pa and 75 Pa of traction for gel stiffness of 0.6 kPa, 1.3 kPa, 2.6 kPa, 6 kPa and 12.7 kPa, respectively. **c,** Average traction of cells treated with 20 μM SMIFH2 in addition to 20 μM BBS as a function of a gel stiffness. **d,** Representative traction vector fields (top) and traction magnitude maps (bottom) of SMIFH2- and BBS-treated cells. Arrow scale: 5 Pa, 15 Pa, 20 Pa, 30 Pa and 50 Pa of traction for gel stiffness of 0.6 kPa, 1.3 kPa, 2.6 kPa, 6 kPa and 12.7 kPa, respectively. **e,** Average traction of cells treated with 1 μM Latrunculin-A (Lat-A) in addition to 20 μM BBS as a function of a gel stiffness. **f,** Representative traction vector fields (top) and traction magnitude maps (bottom) of Lat-A and BBS-treated cells. Arrow scale: 3 Pa, 5 Pa, 7 Pa, 10 Pa and 25 Pa of traction for gel stiffness of 0.6 kPa, 1.3 kPa, 2.6 kPa, 6 kPa and 12.7 kPa, respectively. Power-law curve fits (Traction = b*(Stiffness)^{c}) were added in **(a)**, **(c)** and **(e)** (See Supplementary Table 1 for fit parameters). Scale bar: 10 μm. **g**, Normalized average traction of BBS-treated cells (white) and CK666-BBS (yellow). Bar with error bars: mean ± s.e.m., *: $p<0.05$, **: $p<1\times10^{-10}$, ***$p<1\times10^{-30}$ by Mann-Whitney U test. **h,** Normalized average traction of CK666-BBS -(yellow), SMIFH2-BBS- (dark grey) and Lat-A-BBS-treated cells (light grey). Error bars: s.e.m. *$p<0.05$, **$p<1\times10^{-10}$, ***$p<1\times10^{-20}$ by Kruskal-Wallis ANOVA test with Dunn's post-hoc analysis. **i**, A plot of curve fits of average traction as a function of the stiffness for all conditions.

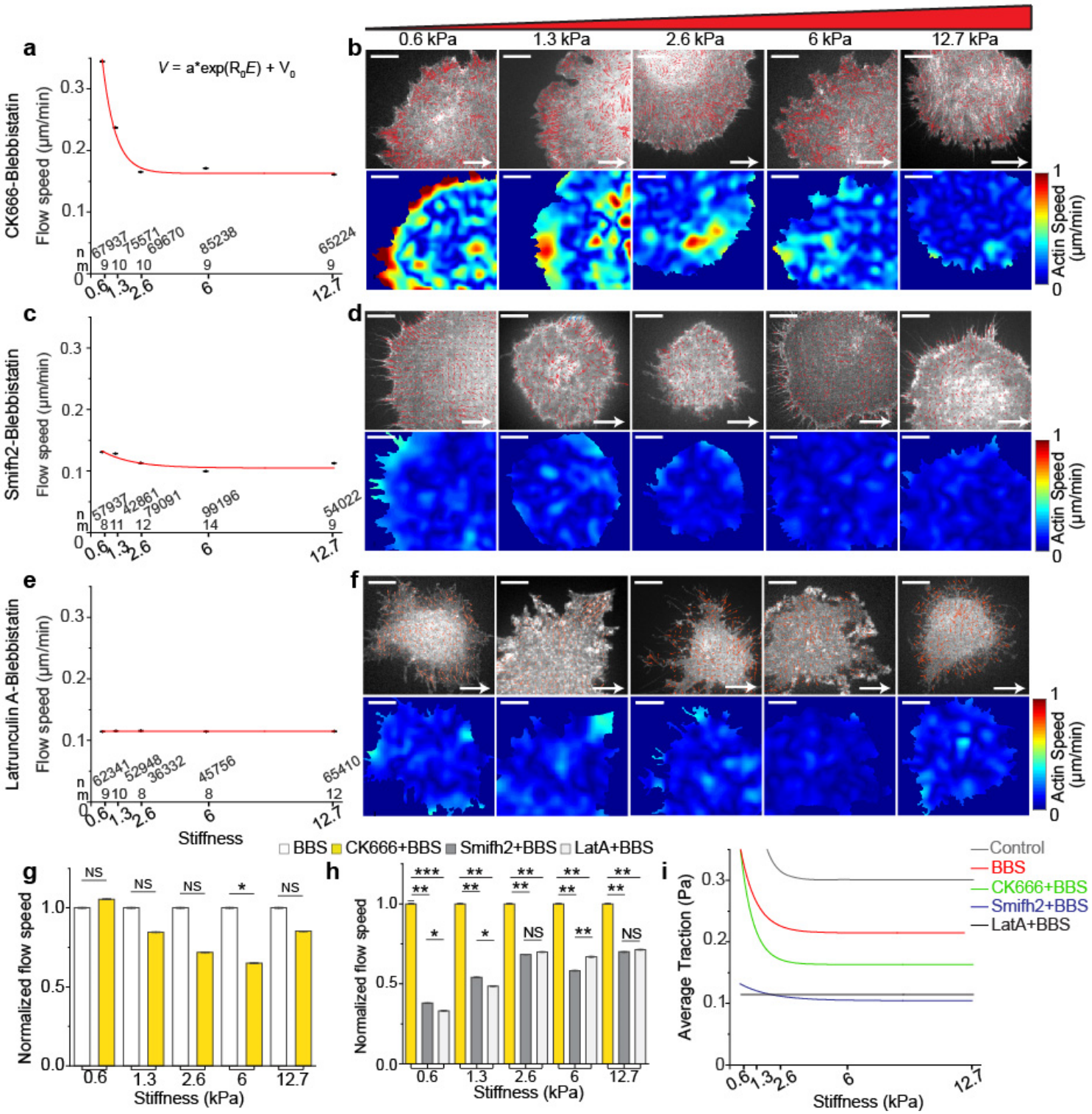

Figure 3

Myosin-independent F-actin retrograde flow is still stiffness-dependent in the absence of Arp2/3 but becomes negligible in the absence of formin and actin polymerization. a, Average F-actin flow speed as a function of the gel stiffness of CK666-BBS treated cells (red, *n* = 9, 10, 10, 9, 9 cells for increasing stiffness, collected from *m* = 67937, 75571, 69670, 85238, 65224 windows). Markers with error bars: mean ± s.e.m. **b,** Representative interpolated flow vectors (top) and speed maps (bottom) of SNAP-actin of CK666-BBS-treated fibroblasts on 0.6 kPa, 1.3 kPa, 2.6 kPa, 6 kPa and 12.7 kPa gel. Arrow scale: 3

μm/min of actin flow. **c,** Average F-actin flow speed as a function of the gel stiffness of SMIFH2-BBS-treated cells (red, *n* = 8, 11, 12, 14, 9 cells for increasing stiffness, collected from *m* = 57937, 42861, 79091, 99196, 80533, 54022 windows). **d,** Representative interpolated flow vectors (top) and speed maps (bottom) of SNAP-actin of SMIFH2-BBS-treated fibroblasts on 0.6 kPa, 1.3 kPa, 2.6 kPa, 6 kPa and 12.7 kPa gel. Arrow scale: 1 μm/min of actin flow. **e,** Average F-actin flow speed as a function of the gel stiffness of Lat-A-BBS treated cells (red, *n* = 9, 10, 8, 8, 12 cells for increasing stiffness, collected from *m* = 52341, 52948, 36332, 45756, 65410 windows). A negative exponential function ($V= a*\exp(R_0E) + V_0$) was used for flow speed vs stiffness plots in **(a), (c)** and **(e)** (See Supplementary Table 2 for fit parameters). **f,** Representative interpolated flow vectors (top) and speed maps (bottom) of SNAP-actin of Lat-A-BBS-treated fibroblasts on 0.6 kPa, 1.3 kPa, 2.6 kPa, 6 kPa and 12.7 kPa gel. Arrow scale: 1 μm/min of actin flow. scale bar: 10 μm**. g**, Normalized actin speed of BBS (white) and CK666-BBS (yellow) treated cells for each corresponding stiffness. *: $p<0.05$, **$p<1\times10^{-20}$, ***$p<1\times10^{-30}$ by Mann-Whitney U test. **h,** Normalized actin speed of CK666-BBS- (yellow), SMIFH2-BBS- (dark grey) and Lat-A-BBS-inhibited cells (light grey). *$p<0.05$, **$p<1\times10^{-20}$, ***$p<1\times10^{-30}$ by Kruskal-Wallis ANOVA test with Dunn's post-hoc analysis. **i,** A plot of curve fits of actin flow speed as a function of the stiffness for all conditions for comparison purpose.

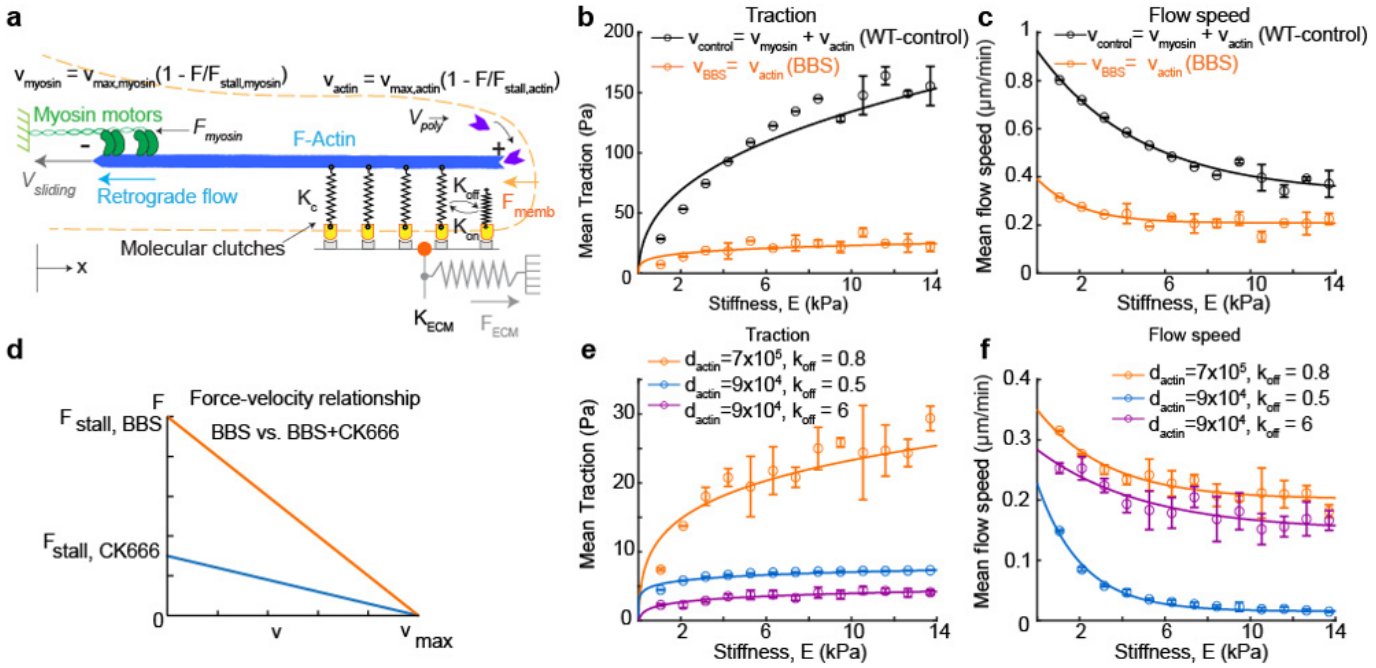

Figure 4. A molecular clutch model assuming rigid actin flow insufficiently explains Arp2/3's role in stiffness-dependent force-flow behaviors. a, A schematic of the molecular clutch model modified with addition of actin polymerization. Actin polymerization-powered retrograde flow velocity as a function of force, $v_{actin} = v_{max,actin}\left(1 - F/F_{stall,actin}\right)$, was added to the myosin motor-generated actin retrograde flow velocity, $v_{myosin} = v_{max,myosin}\left(1 - F/F_{stall,myosin}\right)$. Myosin-independent, stiffness-dependent traction was simulated by considering only v_{actin} without v_{myosin} (see Supplementary Note 2 for details). **b,c,** Simulated results of traction **(b)** and actin flow speed **(c)** as a function of a substrate stiffness. WT-control (*black*) was simulated using both $v_{myosin} + v_{actin}$ but BBS (*orange*) using only v_{actin}. Traction data in **(b)** were fitted using a power law function, i.e., $f = aE^b$ where a = 60.8 and b = $0.38\text{x}10^{-10}$ for WT-control and a = 6.650 and b = $0.14\text{x}10^{-10}$ for the BBS condition. Flow speeds in **(c)** were fitted using a negative exponential relationship, $V = a * exp(R_0E) + V_0$ where a = 0.60, R_0 = -0.21, V_0 = 0.33 for WT-control and a=0.18, R_0= -0.50, V_0=0.21 for the BBS condition. **d,** A force-velocity relationship of actin-polymerization-powered retrograde flow, modeled for actin with (*orange*) and without (*blue*) Arp2/3. Lower stall force ($F_{stall,CK666}$) was assumed for a flow in cells without Arp2/3 and myosin activities than the one ($F_{stall,BBS}$) with Arp2/3. The stall force was modeled to be a function of a local actin density, d_{actin}. **e,f,** Simulated results of traction **(e)** and actin retrograde flow **(f)** as a function of stiffness in BBS (*orange*) and CK666-BBS conditions (*blue, magenta*). CK666-BBS (*blue*) were simulated using lower actin density (d_{actin}: 9×10^4) than BBS condition (d_{actin}: 7×10^5), thus $F_{stall,CK666} < F_{stall,BBS}$ while having low off-rate, K_{off}= 0.8, for clutch binding. CK666-BBS (*purple*) traction and retrograde flow were simulated with high off-rate, K_{off}= 6. Traction data was fitted using power law curve, $f = aE^b$, where where a = 0.2, b = 0.3×10^{-10} for BBS; a = 15.3, b = 0.05×10^{-10} for CK666-BBS; a=12.2, b=0.06×10^{-10} for CK666-BBS-slip. Flow speed was fitted using a negative exponential relationship, $V = a * exp(R_0E) + V_0$ where a = 0.61, R_0 = -0.22, V_0 = 0.33 for BBS; a = 0.21, R_0 = -0.48, V_0 = 0.02 for CK666-BBS (*blue*); a = 0.15, R_0 = -0.30, V_0 = 0.20 for CK666-BBS-slip (*purple*).

Figure 4

See image above for figure legend

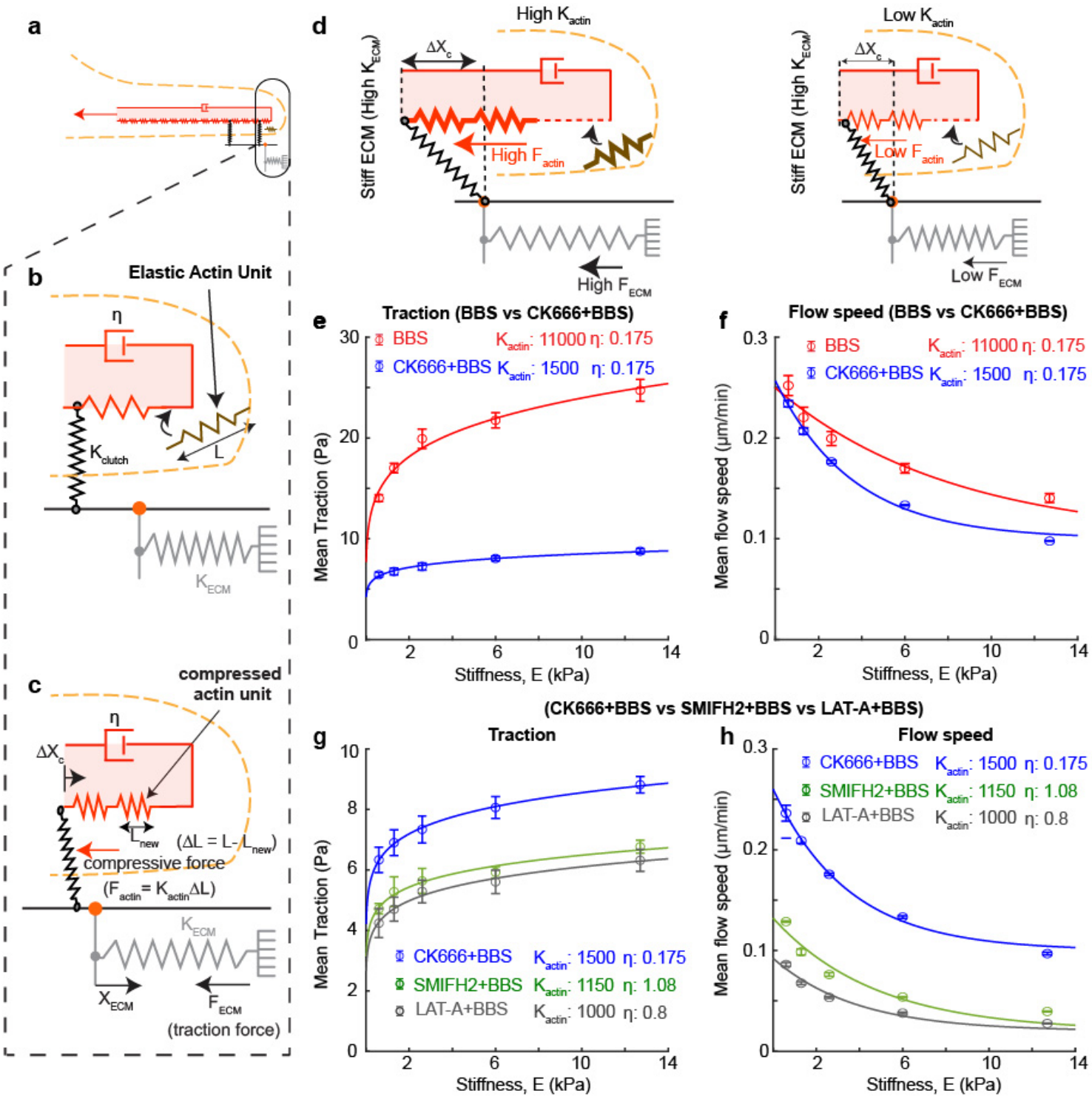

Figure 5

Actin-elasticity-based, actin-polymerization-powered molecular clutch model. a, An overview of the new molecular clutch model that models F-actin as a viscoelastic material. b, c, Magnified views of a cell leading edge before (b) and after (c) addition of an elastic actin unit at a polymerizing tip. The elasticity of an elastic actin unit, Kactin, is an meso-scale modulus and comes from the architecture and morphology of actin fiber network in addition to thickness of individual fibrils and fibers. The added actin unit leads to compressive force, F_{actin}=K_{actin} ΔL, by the boundary conditions at the membrane tension

(right) and at the clutch (left) where ΔL is the change in length of individual actin units. The membrane was assumed to be a rigid wall (see Supplementary Fig. 3 for justification). The compressive force displaces the clutch and is transmitted to the substrate as traction, FECM. The displacement and the force balance are damped by a viscous damper, η, in the actin. D, Illustration that compares the model with high (left) vs. low (right) actin elasticity, Kactin. With high Kactin, addition of a new actin unit results in high force, Factin, which leads to high clutch displacement, Δxc, and thus high traction, FECM. With low Kactin, however, addition of the same original length of the actin unit creates only small Δxc and small FECM because it is compressed more easily. E,f, Model prediction for traction (e) and retrograde flow speed (f) of BBS- (red) and CK666-BBS-treated cells (blue). Note that the only difference between the two conditions is Kactin, 11,000 (BBS) vs. 1000 (CK666-BBS). Traction data was fitted using power law curve, f=aE^b, where a = 16.098 and b = 0.173 for BBS and a = 6.650 and b = 0.106 for CK666-BBS. Flow speed was fitted using a negative exponential relationship, V= a*exp(R_0 E) + V_0 where a = 0.150, R0 = -0.123, V0 = 0.10 for BBS and a= 0.157, R0 = -0.227, V0 = 0.10 for CK666-BBS. G,h, Model prediction for traction (g) and retrograde flow (h) of CK666-BBS- (blue), SMIFH2-BBS- (green) and LatA-BBS-treated cells (black). CK666-BBS was simulated using Kactin = 1500 with a viscosity = 0.175. SMIFH2-BBS and LatA-BBS conditions were simulated using Kactin = 1150 and = 1.08, and Kactin = 1000, viscosity = 0.8, respectively. Traction data was fitted using a power law curve, $f=aE^b$, where a = 6.675, b = 0.108 for CK666-BBS; a = 5.032 and b = 0.110 for SMIFH2-BBS; a = 4.561 and b = 0.126 for LatA-BBS. Flow speed was fitted using a negative exponential relationship, $V= a*\exp(R_0 E) + V_0$ where a = 0.160, R0 = -0.284, V0 = 0.1 for CK666-BBS; a = 0.112, R0 = -0.211, V0 = 0.002 for SMIFH2-BBS; a = 0.072, R0 = -0.261, V0 = 0.02 for LatA-BBS.

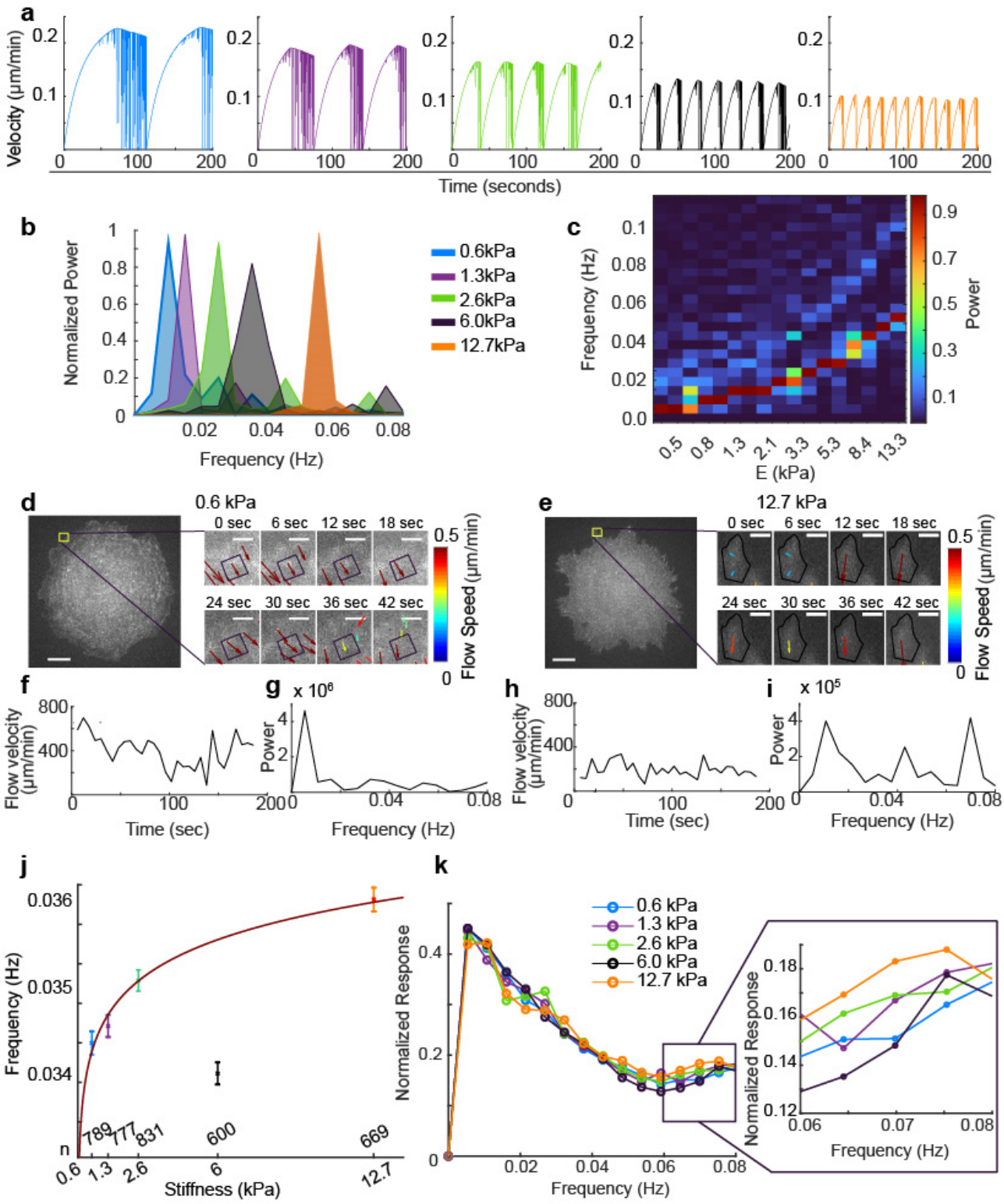

Figure 6

Both model and experiments show that actin flow speed frequency increases with the substrate stiffness. A, Actin flow velocity simulated using actin-elasticity-based clutch model as a function of time on substrates with increasing stiffness, i.e., 0.6 kPa (blue), 1.3 kPa (purple), 2.6 kPa (green), 6.0 kPa (black) and 12.7 kPa (orange). Note that more frequent unclutching events, represented by velocity drop to zero, occurs as the stiffness increases. B,c Frequency analysis of the simulated time-series of velocities with a

power spectrum distribution plot (b) and 2D-histogram of frequency power as a function of stiffness (c). d,e, Representative images of SNAP-SiR647 actin in 3T3 fibroblasts treated with BBS on soft (0.6 kPa) (d) and stiff (12.7 kPa) substrates (e). Right: Montage of SNAP-actin over time with color-coded flow vectors in the yellow-boxed window on the full image. F,g,h,i, Time-series plots of flow velocities (f,h) and power of the flow frequency (g,i) of a cell on a 0.6 kPa gel (f,g) vs. on a 12.7 kPa gel (h,i), sampled from 2×2 μm window in (d) and (e), respectively. J, Average frequencies of hundreds of windows of multiple cells as a function of stiffness. The numbers of windows, n, are denoted on top of x-axis. The numbers of cells per stiffness are: 7, 9, 9, 9, 9 cells for increasing stiffness. A power law curve, $f=aE^b$, was used to fit the observed data, where a = 0.003469 ± (3.5x10-4) and b = 0.01767 ± 0.0073 with R2 = 0.9817. The 4th data point was excluded as an outlier, i.e., outside of 1.5 standard deviation of the output data. K, Normalized power spectra of all windows of cells in all five stiffness conditions. Right: Zoomed-in view of the normalized power spectra in high frequency regime (0.06 – 0.08 Hz). Note the higher power of high stiffness-related actin flow frequency (e.g., 12.7 kPa) than low stiffness-related actin flow frequency in the high frequency regime.

Supplementary Files

This is a list of supplementary files associated with this preprint. Click to download.

- suppmov1.avi
- suppmov2.avi
- suppmov3.avi
- suppmov4.avi
- suppmov5.avi
- suppmov6.avi
- suppmov7.avi
- suppmov8.avi
- suppmov9.avi
- suppmov10.avi
- suppmov11.avi
- suppmov12avi.avi
- suppmov13.avi
- suppmov14.avi
- suppmov15.avi
- suppmov16.avi
- suppmov17.avi
- suppmov18.avi

- suppmov19.avi
- suppmov20.avi
- suppmov21.avi
- suppmov22.avi
- suppmov24.avi
- suppmov25.avi
- Supplementaryinformation.docx